**HEFAT2014**
**10th International Conference on Heat Transfer, Fluid Mechanics and Thermodynamics**
**14 – 16 July 2014**
**Orlando, Florida**

# NUMERICAL STUDY OF THE TRANSIENT CHARACTERISTICS OF ABLATIVE HYPERSONIC FLOW FIELDS

Zeng M.*, Liu J., Xu D. and Zhang W.
*Author for correspondence
College of Aerospace Science and Engineering,
National University of Defense Technology,
Changsha, Hunan, 410073,
P.R.China,
E-mail: ming_z@163.com

## ABSTRACT

The transient characteristics of the reentry flow field with graphite ablation are investigated through numerical simulation. The governing equations for the flow field are Navier-Stokes equations with thermo-chemical non-equilibrium, and that for the heat-shield is the unsteady heat equation. 16-species are considered, thermal non-equilibrium and the coupling of vibration and chemical reactions are described with the two-temperature model. The simulation is performed on a sphere with radius of 1m at a free-stream speed of 10km/s and an altitude of 65km, where the thickness of the heat shield is set to 0.05m, 0.1m, and 0.2m, respectively. The analyses are conducted about not only the time evolutions of the flow field properties and the shield temperature distribution, but also the effects of the shield thickness on them.

## INTRODUCTION

Ablative thermal protection systems are often used in the reentry missions when the flight speeds are above 10 km/s. The chemical reactions or phase change of the surface materials may affect the properties of the flow field around the reentry body, such as the distributions of the temperature, the heat flux, the species mass fraction, and the ionization or radiation properties. So the study of the reentry flow field with ablation is significative in the reentry aerodynamics.

The ablation process involves the interaction between the flow field and the heat shield. The extensive study of ablation may be classified into two categories, one emphasizes on the heat shield, aiming at different kinds of material, studying the chemical kinetics of the material, the heat conduction or pyrolysis process in the heat shield, and so on. The other emphasizes on the flow field, carrying through detail simulation and analysis of the ablative hypersonic flow fields over wide range of Mach numbers and flight altitudes.

Among the study emphasizing on the heat shield, there are investigations on the chemistry model for carbon-based material [1, 2], and the dynamics of pyrolysis gas [3, 4]. Ayasoufi developed a computer program which takes into account in-depth pyrolysis; surface recession; nonequilibrium chemistry in the flow of pyrolysis gases through a variable porosity char; and thermal non-equilibrium between the char and the pyrolysis gases [5]. Based on the existing experimental and numerical results, Shankar analyzed the uncertainty of the surface ablation model for nylon-phenolic resin material, the effects of the speed of pyrolysis gas, and the different dynamic models[6]. Ewing developed a numerical method to solve one-dimensional ablation heat transfer problems, which can model not only the traditional ablation effects, such as heat transfer, material decomposition, pyrolysis gas permeation and thermochemical surface erosion, but also the nontraditional complex ablation phenomena, such as the material swelling and the mechanical erosion [7].

Among the study emphasizing on the flow field properties, the representative numerical simulations and analyses aiming at the flow field with carbon-based material ablation are: the simulation of the flow fields over sphere and sphere-cone with graphite heat shield at free-stream velocities of 8km/s and 10km/s performed by Keenan [8, 9], the simulation of the super-orbital re-entry flow field with ablation over MUSES-C at a velocity of 11.6km/s and an altitude of 64km performed by Suzuki [10], the analysis performed by Gao about the effects of carbon-carbon or carbon-phenolic ablation on the flow field and wake properties of sphere and sphere-cone at velocities of 7.5 to 8km/s [11], the investigation performed by Tisserai on the ablative flow field of the double-cone and the ablation effects on wall pressure and heat flux at a Mach number of 8.87 in LENS-I shock tunnel [12], the numerical study performed by Bianchi on the graphite ablation flow over a sphere-cone at a free-stream velocity of 5354m/s and an enthalpy of 27MJ/kg in an arc-jet tunnel [13]. The newly study of ablation-flow-field

coupling relevant to the Orion heat shield performed by Johnston[14], which applies a 32-species thermo-chemical nonequilibrium model that including C, H, O, N, and Si-containing species, allows the char ablation rate to be computed as part of the solution, and compares the coupled results with the uncoupled results.

On the basis of the previous ablation study, the present work examines the transient characteristics of the reentry flow field during the unsteady ablation of graphite heat shield. Taking a one meter nose radius sphere at a free-stream velocity of 10km/s and an altitude of 65km as an example, the transient process of the flow field is numerically simulated with an approximate time-accurate scheme. The time evolutions of the flow field properties as well as the effects of ablation and the thickness of the heat shield on the flow field are investigated.

## NOMENCLATURE

| | | |
|---|---|---|
| $C_p$ | [J/kgK] | Heat capacity |
| $C_s$ | [-] | Species mass fraction |
| $D$ | [m$^2$/s] | Diffusion coefficient |
| $E$ | [J/m$^3$] | Total energy per unit volume |
| $h$ | [J/kg] | Enthalpy |
| $H$ | [J/kg] | Total enthalpy |
| $k$ | [W/mK] | Thermal conductivity |
| $\dot{m}$ | [kg/m$^2$s] | Mass flux |
| $n$ | [m] | Normal distance from the wall |
| $\vec{n}$ | [-] | Surface unit normal vector |
| $q$ | [W/m$^2$] | Heat flux |
| $R$ | [m] | Radius of the sphere |
| $T$ | [K] | Temperature |
| $x$, $r$ | [m] | Axisymmetric coordinates |

Special characters

| | | |
|---|---|---|
| $\varepsilon$ | [-] | Emissivity, 0.9 |
| $\sigma$ | [W/m$^2$K$^4$] | Stefan-Boltzmann constant |
| $\rho$ | [kg/m$^3$] | Density |

Subscripts

| | |
|---|---|
| $n$ | Nose |
| $s$ | Species value |
| *solid* | Solid heat shield material |
| $w$ | Wall surface |

## THERMOCHEMICAL MODEL AND GOVERNING EQUATIONS

The high temperature air is composed of 10 species in the study: $N_2$, $O_2$, NO, N, O, $NO^+$, $N_2^+$, $O^+$, $N^+$, $e^-$. As graphite ablation occurs, the following species may also appear in the flow field: CO, $CO_2$, C, $C_2$, $C_3$, CN. 29 chemical reactions [1, 15] are considered for these 16 species. The two-temperature (translational/rotational and vibrational temperature) model is used to describe thermal non-equilibrium and the coupling of vibration and chemical reactions. The thermodynamic and transport properties of the gas mixture are calculated with the method described in [1]. The surface reactions take into account the process of thermo-chemical ablation due to both oxidation and sublimation [8, 9].

The governing equations for the flow field are the axisymmetric Navier-Stokes equations coupled with the vibrational and chemical kinetics, which are solved to obtain the steady state solution of the flow field. The details of the flow field governing equations are described in [16].

The governing equation set for the heat shield can be reduced to one equation [8] if the density of the solid is assumed to remain constant, the stress and strain within the material are neglected and no internal diffusion or velocities are permitted. The only one equation is the unsteady heat equation which expresses the conservation of energy as

$$\frac{\partial E}{\partial t}+\frac{\partial q_x}{\partial x}+\frac{1}{r}\frac{\partial\left(rq_r\right)}{\partial r}=0 \tag{1}$$

where

$$E=\rho_{solid}c_{p,solid}T \tag{2}$$

$$q_r=-k_{solid}\frac{\partial T}{\partial r},\quad q_x=-k_{solid}\frac{\partial T}{\partial x} \tag{3}$$

## ABALTIVE SURFACE BOUNDARY CONDITIONS

To couple the flow field to the heat shield during ablation, mass balance and energy balance must be satisfied at the surface. The surface mass balance for each species is

$$-\left(\rho D_s\nabla C_s\bullet\vec{n}\right)_w+\dot{m}_w C_{s,w}=\dot{m}_{s,w} \tag{4}$$

where the first term on the left side is the diffusion of species, $\vec{n}$ is the surface unit normal vector (away from the wall), $\dot{m}_w$ is the total mass flux at the surface, and $\dot{m}_{s,w}$, the mass flux of species $s$ per second, is determined from the surface thermo-chemistry [8]. There are 15 surface mass balance equations in this study with the assumption of quasi-neutral plasma.

The surface energy balance is expressed as

$$-q_w+q_{cond,w}-\varepsilon\sigma T_w^{\,4}+\dot{m}_w\left(h_{solid,w}-H_w\right)=0 \tag{5}$$

where $q_w$ is the heat flux to the flow from the wall, which contains both the heat conduction and the diffusive chemical heat flux, $\varepsilon\sigma T_w^{\,4}$ is the re-radiation of heat into the flow, $q_{cond,w}$ is the heat flux conducting energy to the surface from the heat shield

$$q_{cond,w}=-\left(k_{solid}\nabla T_{solid}\bullet\vec{n}\right)_w \tag{6}$$

which is related to the temperature distribution in the heat shield. The fourth term in (5) is the removal of energy from the surface due to mass removal.

To set boundary conditions for the pressure and velocity, an assumption is made that blowing occurs only normal to the body. This allows the pressure and velocity to be related through the equation of state and the conservation of mass for one-dimension. Moreover, the normal gradient of pressure at the surface is assumed to be zero. Then, from these surface boundary conditions, the surface temperature, pressure, species densities and injection velocities can be determined as part of the solution.

## NUMERICAL METHOD

A fully implicit finite difference method is used in the calculation, all inviscid terms are discretized with AUSMPW+

scheme and the viscous terms are discretized with center difference scheme, the implicit parts of the differential equations are disposed in two steps with LU-SGS approach.

The unsteady heat equation is solved using a forward time, centered space scheme. The adiabatic conditions are used for the inner wall of the ablator. The centreline condition is set to be reflective.

The transient flow field during the ablation process of heat shield is simulated in an approximate time-accurate manner. Considering the fact that the time scale for the flow field to adjust to changes in the surface conditions is far less than that for the ablator change, the governing equations for the flow field and the heat shield are solved following a partial decoupling procedure: First set an initial temperature within the ablator and hold it constant while obtaining a converged flow field solution. Then the heat flux to the ablator is computed and held constant during the unsteady heat conduction process in the heat shield for an ablator time step, after which a new surface temperature results. The process is advanced such to obtain the approximate time-accurate transient flow field. In the limit of small ablator time steps, this procedure is time accurate and the flow field is fully coupled to the ablator. For the graphite material used in the following simulations, an ablator time step of 0.2s is small enough for the partial decoupling procedure to maintain the correct coupling of the physical process.

## RESULTS AND ANALYSIS

The simulation of the transient as well as the steady-state (i.e., without heat flux into the ablator) flow field are performed on a sphere with radius of 1m at a free-stream velocity of 10km/s and an altitude of 65km. The thickness of the heat shield is set to 0.05m, 0.1m, and 0.2m, respectively. The initial surface and ablator temperature are both set to 500K, no ablation or catalyze processes occur initially, and the flow field is initialized as the steady-state one under the initial condition. The time procedure is run for more than 1200s from the initialization stage. An ablator time step of 0.2s is used.

The results are presented in two sections. In the first section, the transient characteristics of the flow field properties and the temperature distribution in the heat shield are analyzed, where the case with 0.2m heat shield is taken as an example. In the second section, the effects of the shield thickness are investigated by comparisons among the three cases with shields of different thicknesses.

### Analysis of the Flow Field with 0.2m Heat Shield

The surface temperature, the heat flux to the wall and the non-dimensional mass flux [ $\bar{m}_w = \dot{m}_w / (\rho_\infty V_\infty)$ ] are given in Figure 1 to 3. At the initialized stage, when the surface temperature is 500K and there is no ablation or catalyze process, the stagnation heat flux is about 1.5 MW/m$^2$. The high heat flux leads to the ablation of the heat shield. At first the heat flux grows dramatically with ablation due to the catalytic reactions for $O_2$, CO and $CO_2$, which result in heat release near the surface, at $t$=1s, the stagnation heat flux attains 12 MW/m$^2$. As the ablation process carries on, the removal of surface material accompanied with the removal of energy begins, as well as the heat conduction into the shield. As a result, the surface temperature increases and the heat flux from the flow to the wall decreases rapidly. At $t$=5s, the stagnation temperature rises to 1200K and the heat flux decreases to 6.4 MW/m$^2$. The surface temperature near the stagnation point reaches 2200K at $t$=100s, then it increases slightly, even at $t$=1680s, it climbs to only 2580K, which is still 40K lower than the steady-state value. Away from the stagnation point region, the surface temperature grows more slowly, it only attains around 750K after $t$=1000s, about 400K lower than that of the steady-state ablation case. As the time advances, both the heat flux and the mass flux decrease gradually, but the changing processes become very slow after 50s. It takes 200s for the heat flux while only 100s for the mass flux to approach the steady-state value. And after that, though the surface temperature still grows with time, both the heat flux and the mass flux change minimally.

The ablation products exist mainly in the boundary layer. The dominant ablation species is CO, next is C and CN, then $CO_2$. As departing from the stagnation region, the temperatures in either the shock layer or the boundary layer decrease, so does the surface temperature. As a result, the mass fraction of $CO_2$ increases, and exceeds that of CN along ray at 90°. $C_2$ and $C_3$ are trace species, even in the vicinity of the stagnation point, their mass fractions are in the order of $10^{-5}$.

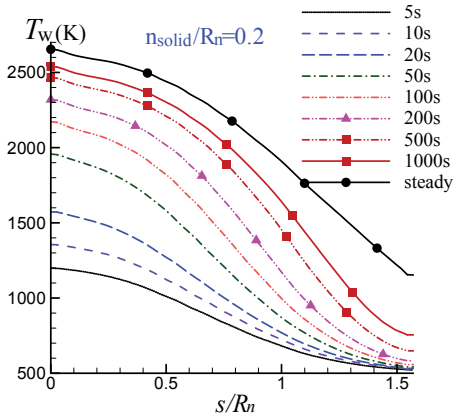


**Figure 1** Time evolution of wall temperature distribution

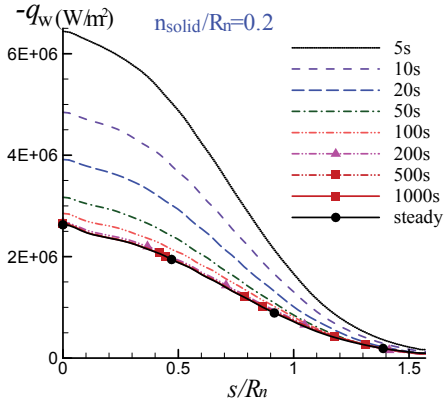


**Figure 2** Time evolution of wall heat flux distribution

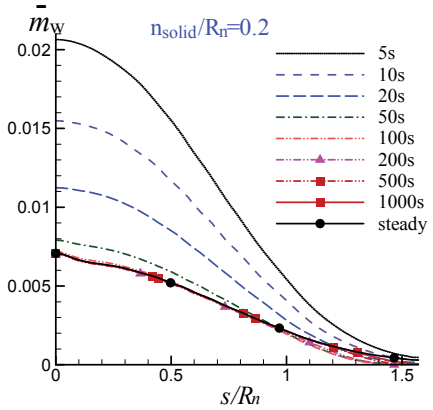


**Figure 3** Time evolution of wall mass flux distribution

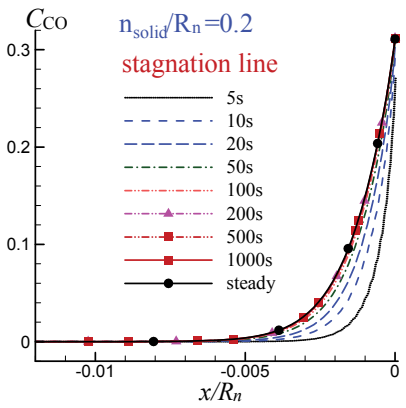


**Figure 4** Time evolution of $C_{CO}$ distribution along stagnation line

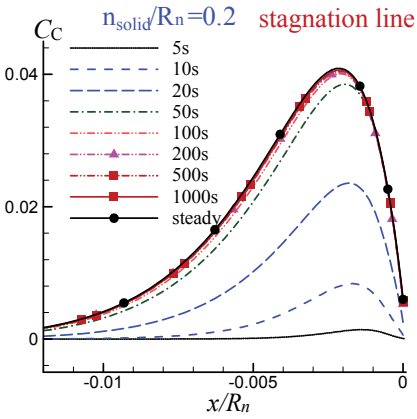


**Figure 5** Time evolution of $C_C$ distribution along stagnation line

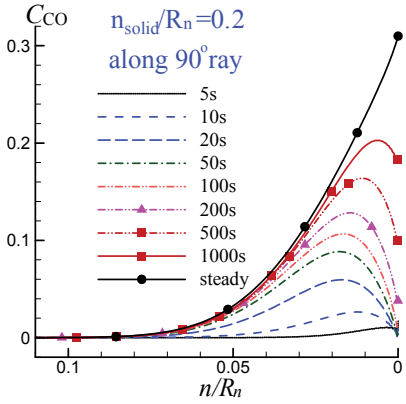


**Figure 6** Time evolution of $C_{CO}$ distribution along ray at 90°

Here the distribution of the mass fraction of the two major carbon species namely CO and C are examined in detail. In Figure 4 and Figure 5 the mass fractions along the stagnation line in the boundary layer are given for several time levels. It can be seen that as the ablation begins, CO is formed at the wall substantially and reaches a mass fraction of 0.3. But as the flow departs from the wall, CO mass fraction undergoes a steep decrease, which is due to the reactions between CO and O or N as well as the dilution of the air species. As can be seen in Figure 5, the mass fraction of C rises as departing from the wall, and peaks at $0.002R_n$ from the wall, (by the way, the boundary layer thickness is about $0.011R_n$), and the peak value increases swiftly with time. There is no noticeable change in the mass fraction of the ablating species along the stagnation line after $t$=100s.

The distributions of mass fraction along ray at 90° are shown in Figure 6 and Figure 7. The heat flux here is much lower than that in the stagnation region, and the surface temperature increases rather slowly, only from 500K to 556K at $t$=100s, while for the steady-state case the surface temperature here is about 1150K. So the mass fractions of the ablation species here have substantial difference with the steady-state case. In the first 5 seconds, CO is formed at the wall, but it increases a little after departing from the wall and reaches a peak near the wall. At $t$=100s, the peak value is 0.1. The rise in CO mass fraction may attribute mainly to the flow from the nose region, because at the low temperature here the formation of CO is minimal. For the steady-state case, large amount of CO is formed at the wall, but the mass fraction decreases as departing from the wall. The mass fraction of C increases with time, in both the transient case and the steady-state case the peak values appear in the boundary layer rather than at the wall. For C mass fraction, the process running to steady-state is not so long as that for CO (in Figure 6), the results at $t$ =200s is very close to the steady-state (in Figure 7).

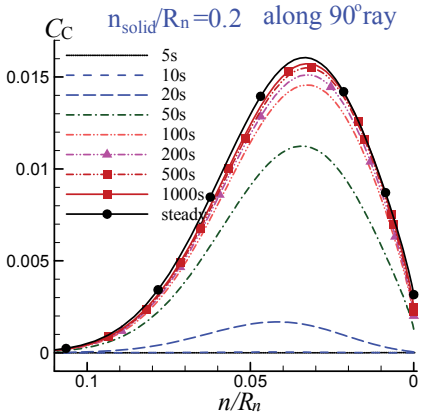


**Figure 7** Time evolution of $C_C$ distribution along ray at 90°

Figure 8 and Figure 9 show the mass fraction contours of CO at 400s and that for steady-state case respectively. The ablation species are limited to the vicinity of the wall, especially in the nose region, where they exist only in half of the boundary layer. After $t$=100s, the mass fraction of CO in the nose region is very close to the steady-state case, but in the back part, even at $t$=400s, it is still lower than the steady-state case. This is consistent with the still low surface temperature here, as can be seen in Figure 1.

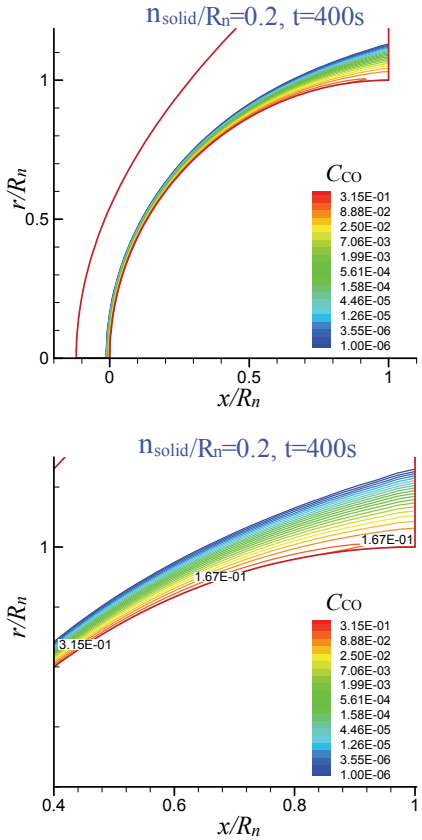


**Figure 8** $C_{CO}$ distribution at $t$=400s

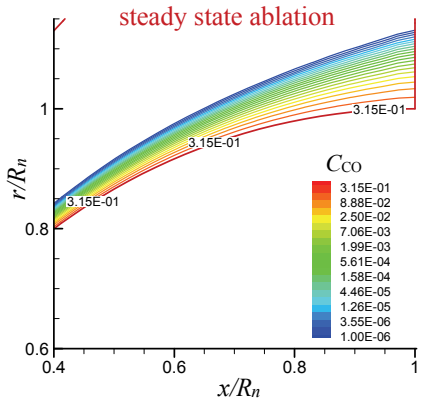


**Figure 9** $C_{CO}$ distribution for steady state ablation

The effects of ablation on the flow field embody mainly on the thermo-chemical properties in the boundary layer. The mass fractions of the atoms (monatomic O and N) and the ions ($NO^+$, $N_2^+$) decrease near the wall because of ablation, while the recombination of N is facilitated by the ablation. This characteristic is observed in Figure 10 and Figure 11, which give the distributions of mass fraction of N and $N_2^+$ along the stagnation line. The ablation species facilitate the recombination of atoms and reduce their mass fractions. This leads to the further decrease of $NO^+$, $N_2^+$, as N and O are the reactants of the recombination-ionization reactions, which produce $NO^+$, $N_2^+$.

The centreline temperature within the heat shield is given for various time levels in Figure 12. The heat conduction process in the heat shield is fairly slow. For example, at $t$=100s, the temperature reaches 2200K at the surface, while attains only 920K at the inner 0.05m from the surface and only 590K at 0.1m from the surface. Figure 13 and Figure 14 give the temperature contours in the heat shield at $t$=400s and 1280s respectively, from which we can see that the thermal gradients are still noticeable and the case is far from steady-state.

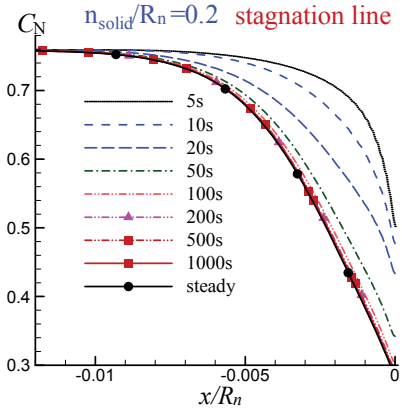


**Figure 10** Time evolution of $C_N$ distribution along stagnation line

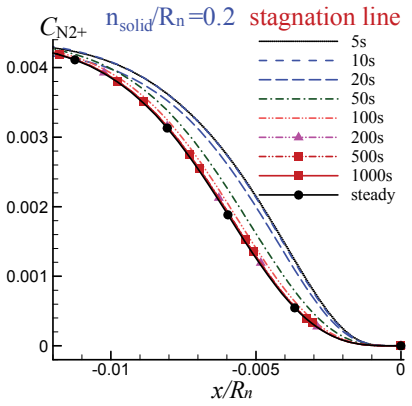


**Figure 11** Time evolution of $C_{N2+}$ distribution along stagnation line

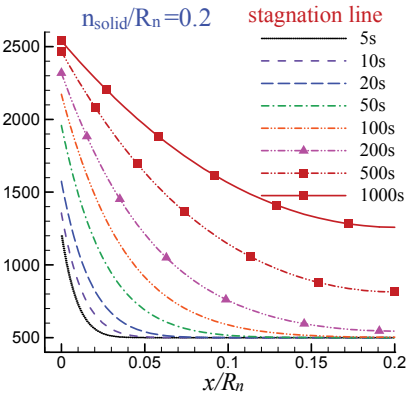


**Figure 12** Time evolution of centerline temperature distribution within the shield

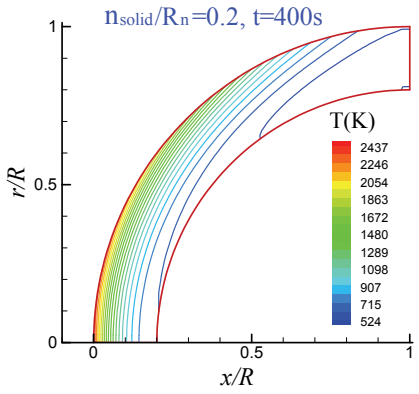


**Figure 13** Temperature distribution in the shield at $t$=400s

### Analysis of the Effects of the Heat Shield Thickness

The heat shield absorbs energy through not only chemical reactions and mass removal of the material, but also heat conduction in the shield itself. The solid material acts as a heat capacity to absorb the conduction heat flux, its temperature rises until attains an even distribution, in other words, arrives at the steady-state. Heat shields of different thickness correspond to different heat capacity, and the time process to run to steady-state gets shorter when the heat shield gets thinner.

Figure 15 gives the time evolution of stagnation temperature for the 3 heat shields with different thickness, 0.05m, 0.1m, and 0.2m, respectively. It takes about 500s for the stagnation temperature of 0.05m shield case to approach the steady-state value, while about 1000s for the 0.1m case. As for the 0.2m case, the stagnation temperature is still 40K lower than the steady-state value even at $t$=1680s. Figure 16 gives the wall temperature distribution at different time levels for 0.05m shield case, which shows that in most region the steady-state is obtained at $t$ =1000s. However, for the 0.2m shield case, even the stagnation temperature is considerably different from the steady-state value, as is noted in Figure 1.

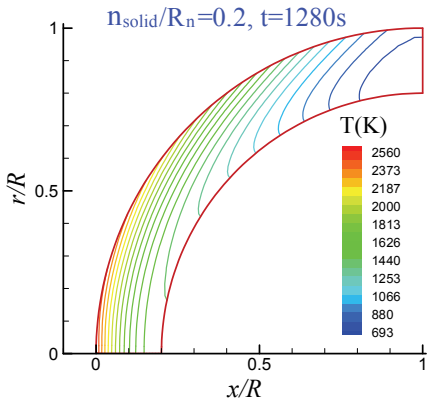


**Figure 14** Temperature distribution in the shield at $t$=1280s

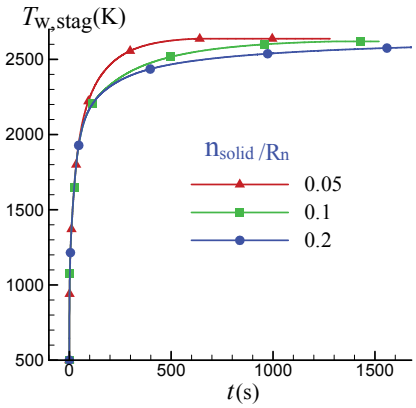


**Figure 15** Time evolution of wall surface temperature at stagnation with heat shields of different thickness

We have known that though it takes rather long time for the wall temperature to attain steady-state value, the mass fractions of the ablating species approach steady-state rapidly. Therefore, the shield thickness can hardly affect the transient processes of the mass fractions along the stagnation line. However, in the back part region the transient processes are fairly long and affected by the shield thickness. Figure 17 shows the

distribution of CO mass fraction along ray at 90° for the case with 0.05m shield, as one can see that the distribution at $t$=1000s is very close to the steady-state case, while for the case with 0.2m shield (shown in Figure 6), the difference with the steady-state case is considerable.

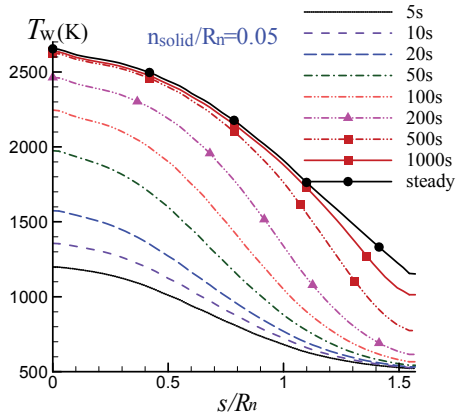


**Figure 16** Time evolution of wall temperature distribution (0.05m heat shield)

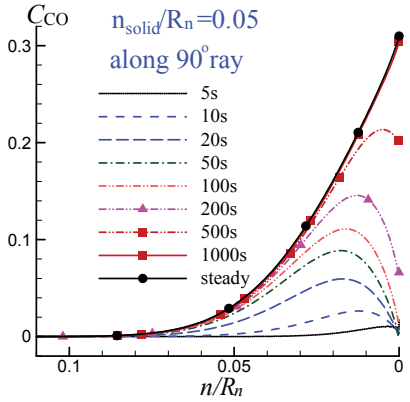


**Figure 17** Time evolution of $C_{CO}$ distribution along ray at 90° (0.05m heat shield)

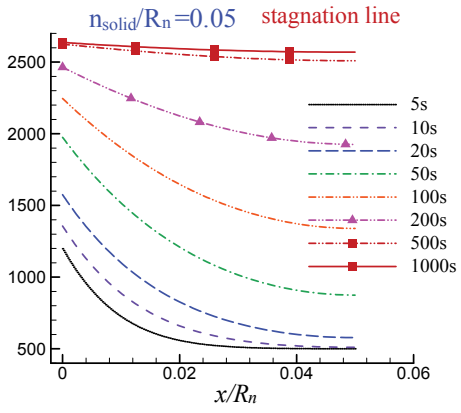


**Figure 18** Time evolution of centerline temperature distribution within the shield (0.05m heat shield)

The centreline temperature distribution within the heat shield with thickness of 0.05m is given for various time levels in Figure 18. The distribution at $t$=500s is fairly even, which approaches the steady-state distribution. Figure 19 and Figure 20 give the temperature contours in the heat shield with thickness of 0.05m and 0.1m at $t$=400s and 1280s respectively. By comparison of Figure 19 and Figure 20 with Figure 13 and Figure 14, the effects of the shield thickness on the transient behaviour of the inner temperature distribution are very clear.

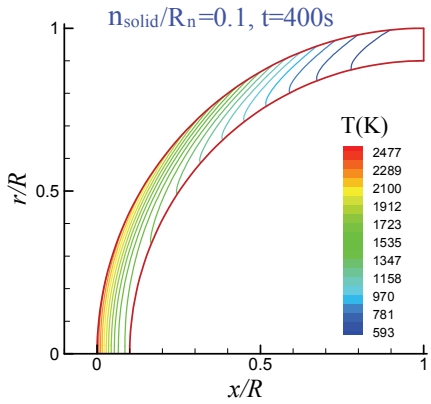


(a) 0.1m heat shield

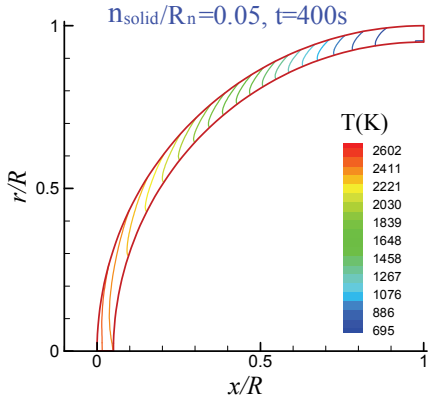


(b) 0.05m heat shield

**Figure 19** Temperature distribution in the shield at $t$=400s (0.1m and 0.05m heat shield)

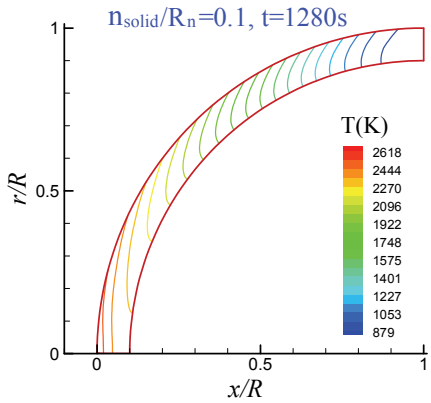


(a) 0.1m heat shield

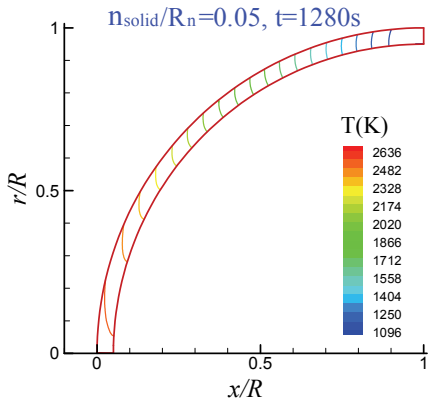


(b) 0.05m heat shield

**Figure 20** Temperature distribution in the shield at $t$=1280s (0.1m and 0.05m heat shield)

## CONCLUSION

In this study, the transient reentry flow field over a sphere model with graphite heat shield is simulated and analyzed. The primary conclusions obtained from the numerical results are:

(1) The heat flux to the wall from the flow is very large initially, which leads to high rate of ablation. The immediate effects of catalytic reactions and oxidation are most significant in the first few seconds of the run. The heat flux and mass flux approach the steady-state values in 100s, while the transient process for the surface temperature is rather long. In the 0.05m shield case, it takes about 500s for the surface temperature at the stagnation point to reach the steady-state value, while at the shoulder the surface temperature is still one-fifth off the steady-state value at that time. As for the case with 0.2m shield, the surface temperature at the stagnation point is 4% lower and at the shoulder is one-third lower than the steady-state value even after 1000s.

(2) The ablation products exist mainly in the boundary layer. The most important ablation species are CO, then C and CN, then $CO_2$. The mass fraction of $CO_2$ increases with the drop of temperature as the flow departs from stagnation. The mass fractions of most ablation species rise with time, in the vicinity of the stagnation point they approach the steady-state values in 100s while the transient processes at the shoulder last about 800s for 0.05m shield case and about 2000s for 0.2m shield case.

(3) The effects of ablation on the flowfield are also limited to the boundary layer, and they are exhibited mainly on the temperature and species mass fraction. The surface reactions lead to the decrease of O, and as the ablation species flow into the boundary layer they induce the reduction of atoms and ions. However, the peak mass fractions of atoms or ions are not affected by ablation because they appear outside the boundary layer. The effects of ablation increase with time, and the process running to steady-state behave similarly to those of the ablation species.

(4) The characteristics of the transient process for the ablation species are similar to those for the heat flux and mass flux. For example, they all approach the steady-state value after 100s, but the surface temperature is still one-fourth lower than the steady-state value at the time. This indicates that the surface influence the flow field through a more integrated mechanism which satisfies surface mass and energy balance rather than simply through surface temperature.

(5) As the flow departs from the stagnation region, the transient process lasts longer, such is the case as the shield becomes thicker. So the numerical results of the flow field with the assumption of steady-state ablation may differ from the real flight case, especially in the region away from the stagnation. The detail simulation of the transient reentry flow field during ablation is necessary for accurate prediction of the real flow field.

## REFERENCES

[1] Park C.， Jaffe R. L., and Partridge H., Chemical-kinetic parameters of hyperbolic Earth entry, *Journal of Thermophysics and Heat Transfer*, Vol. 15, 2001, pp. 76-90

[2] Martin A., Boyd I. D., Cozmuta I., and Wright M. J., Chemistry model for ablating carbon-phenolic material during atmospheric re-entry, *AIAA Paper* 2010-1175

[3] Ahn H. K., Park C., and Sawada K., Dynamics of pyrolysis gas in charring materials ablation, *AIAA paper* 98-0165

[4] Martin A., and Boyd I. D., Simulation of pyrolysis gas within a thermal protection system, *AIAA Paper* 2008-3805

[5]Ayasoufi A., Numerical simulation of ablation for re-entry vehicles, *AIAA Paper* 2006-2908

[6] Shankar B., Uncertainty analysis of surface ablation, *AIAA Paper* 2009-261

[7] Ewing M. E., Numerical modelling of ablation heat transfer, *Journal of Thermophysics and Heat Transfer*, Vol. 27, 2013, pp. 615-631

[8] Keenan J. A., and Candler G. V., Simulation of ablation in Earth atmosphere entry, *AIAA Paper* 93-2789

[9] Keenan J. A., and Candler G. V., Simulation of graphite sublimation and oxidation under re-entry conditions, *AIAA Paper* 94-2083

[10] Suzuki K., Kubota H., Fujita K., and Abe T., Chemical nonequilibrium ablation analysis of MUSES-C super-orbital reentry capsule, *AIAA Paper* 97-2481

[11] Gao T., Dong W., Zhang Q., The computation and analysis for the hypersonic flow over reentry vehicles with ablation. Acta Aerodynamica Sinica. Vol. 24, 2006, pp. 41-45 (in Chinese)

[12] Tissera S., Titarev V., and Drikakis D., Chemically reacting flows around a double-cone including ablation effects, *AIAA Paper* 2010-1285

[13] Bianchi D., Nasuti F., and Onofri M., Aerothermodynamic analysis of reentry flows with coupled ablation, *AIAA Paper* 2011-2273

[14] Johnston C. O., Study of ablation-flowfield coupling relevant to the Orion heat shield, *Journal of Thermophysics and Heat Transfer*, Vol. 26, 2012, pp. 213-221

[15] Blottner F.G. Prediction of electron density in the boundary layer on entry vehicles with ablation. N71-21113, 1971.

[16] Zeng M.， Numerical rebuilding of free-stream measurement and analysis of Nonequilibrium effects in high-enthalpy tunnel. [Ph D Thesis]. Beijing: Institute of Machanics, CAS. 2007 (in Chinese)